Nanoscale

PAPER

View Article Online
View Journal | View Issue

Cite this: *Nanoscale*, 2025, **17**, 27947

The electrocatalytic hydrogen evolution reaction using a heteroatom-doped hollow onion-like fullerene across a wide pH range

Isha Mehta,[a] Anubha Rajput,[b] Purva Yewale,[a] Biswarup Chakraborty *[b] and Sagarika Bhattacharya *[a]

Electrocatalytic hydrogen production from the water splitting reaction can satiate the global future energy demand. Low-dimensional carbon nanomaterials have attracted the attention of researchers due to their low cost, easy synthetic techniques, high mechanical/chemical stability, remarkable electrical conductivity, large specific surface area, and environmentally benign nature. Specifically, hollow Onion-Like Fullerenes (*h-OLFs*) with high porosity can be promising metal-free electrocatalysts for the production of green hydrogen. In this work, we report the hydrothermal synthesis of *h-OLF* in a specific bottom-up method from glucose and sulphanilamide as organic precursors and its subsequent characterization. Upon introducing the *h-OLF* as a carbon-based cathodic material on the 1 cm^2 surface of nickel foam, reasonable hydrogen evolution reaction (HER) activity was observed in non-aqueous media containing different amounts of *p*-toluene sulphonic acid (PTSA), acetic acid (AcOH), sulphate buffer, and dilute HCl as the proton source, giving rise to a very low overpotential (η) of 133 mV to achieve a cathodic current of 10 mA cm^{-2} and long-term HER performance, *e.g.*, 30 000 s, while maintaining j_{HER} > 15 mA cm^{-2} under chronoamperometric conditions. The lowest Tafel slope value and low charge transfer resistance (R_{ct}) indicate the favourable HER electrokinetics of the *h-OLF*. The highest double-layer capacitance (C_{dl}) in the dilute HCl-containing non-aqueous electrolyte further implies maximum exposure of the electrochemically active sites, facilitating proton adsorption ont the surface of the *h-OLF*, showcasing the remarkable HER activity of this unique carbon-based nanomaterial.

Received 18th August 2025,
Accepted 8th November 2025

DOI: 10.1039/d5nr03492b

rsc.li/nanoscale

Introduction

Clean and renewable energy production can sustainably meet the high demand for energy in the future.[1–4] Increasing global energy demand is depleting the conventional energy resources (fossil fuels), while simultaneously increasing pollution.[3,4] Thus, the development of clean, pollution-free, and renewable energy sources is urgently needed due to the limited availability of non-renewable energy sources. However, renewable sources are intermittent and show seasonal dependence; hence, the production of energy from renewable energy sources, *e.g.*, biomass, sun, and wind, has limited applicability.[5,6] In this regard, hydrogen (H_2) energy has emerged as the most suitable alternative due to its abundance, high calorific value, high gravimetric energy density, and non-carbonaceous nature. The generation of green H_2, a low-polluting and highly efficient fuel, can reduce fossil fuel dependence while satisfying the need for future energy requirements without compromising current supply. Currently, 90% of hydrogen is produced by thermal dissociation of water, coal gasification, and methane oxidation at the cost of fossil fuel burning.[7,8] Currently, the production of green hydrogen using the HER, the OER and the ORR stands at nearly 4–5%. Noble metals are highly efficient as catalysts for the HER including Pt,[9] Ir,[10] Pd,[11,12] Os,[13,14] Rh,[15] and Ru[16] because of their low overpotential and high activity. However, their high cost and limited supply prevent their widespread commercialization. HER activity has also been noted with non-precious transition metal compounds, *e.g.* phosphides,[2,17] borides,[18,19] selenides,[20–22] and nitrides[23,24] but most of these suffer poor long-term stability under alkaline and acidic pH conditions and often exhibit potential-driven phase transformations.[25] In recent years, researchers have focused on developing metal-free carbon-based electrocatalysts due to their attractive properties such as environmentally benign nature, large surface area, and low cost. Several carbon-based nanostructured materials, *e.g.*, carbon quantum dots (CQDs),[26] carbon

[a]*Department of Chemistry, National Institute of Technology Raipur, Raipur, Chhattisgarh 492010, India. E-mail: sbhattacharya.chy@nitrr.ac.in*
[b]*Department of Chemistry, Indian Institute of Technology, Delhi, Hauz Khas, New Delhi, 110016, India. E-mail: cbiswarup@chemistry.iitd.ac.in*

Table 1 A comparison table of HER performance in carbon-based materials based on the overpotential and Tafel slope

S. no.	Material	Precursor used	Electrode support for the materials	Overpotential (mV)	Tafel slope (mV dec^{-1})	Ref.
1	Carbon quantum dots	*N*-Methyl pyrrolidone and zeolite	Glassy carbon electrode (GCE)	341	126	38
2	g-C_3N_4 nanoribbons	g-C_3N_4 graphene oxide	GCE	207	54	39
3	Carbon dots	*Citrus medica*	—	268	82	40
4	B-doped graphene	Graphene oxide and BH_3–THF	GCE	450	99	41
5	N,S co-doped graphene	Graphene oxide and thiourea	GCE	322	188	42
6	N-doped graphitic carbon sheets (N-GCSs)	*R. parvifolius* fruit	Carbon cloth	250	198	43
7	Nitrogen-doped multi-walled carbon nanotubes	Polyaniline emeraldine salt and MWNTs (multiwalled nanotubes)	GCE	340	78	44
8	Nitrogen-doped graphene microtubes (N-GMTs)	Glycine and dicyandiamide (DCDA).	GCE	464	116.7	45
9	Heteroatom-doped graphene	Graphene oxide, melamine, and benzene disulfide	Rotating disc electrode	310	120	46
10	*h-OLF*	Glucose and sulphanilamide	NF	133	251	This work

nitrides,[27,28] carbon nanotubes (CNTs),[29,30] carbon nano-onions (CNOs)/hollow Onion Like-Fullerenes (*h-OLF*s),[31,32] and carbon dots,[33] have been employed as metal-free electrocatalysts in the HER. Among all of the allotropes of carbon, *h-OLF*s are the most underexplored materials. In 1992, Iijima and Ugarte first reported *h-OLF*s. Because of their spherical shape, nano-scale size, porosity, low-cost synthesis, stability, and biocompatibility, *h-OLF*s are used in various fields.[34,35] There are various synthesis methods that are used to produce *h-OLF*s, such as thermal annealing, chemical vapor deposition, arc-discharge methods, *etc*., but all of these methods are expensive and operate under high-temperature conditions.[36] Structurally, the *h-OLF* consists of onion-like homocentric graphene shells with multi-layered fullerenes forming the inner core of the material. The performance of these materials can be tuned by the incorporation of active functional moieties on their surface during synthesis. Based on the previous reports, these functional groups present on electro-active carbon materials, as revealed through various spectroanalytical techniques, play an intriguing role in electrocatalysis.[6,37]

In this work, we synthesized hollow -Onion-Like Fullerenes (*h-OLF*s) by the hydrothermal technique in bottom up method from glucose and sulphanilamide in a 2 : 1 ratio at very low operational temperature. The hollow cavity with concentric onion-like layers was visualized by HR-TEM images and the *h-OLF* is characterized through other spectroscopic techniques. The *h-OLF* as a carbon-based nanomaterial was deposited onto nickel foam, and its intrinsic HER activity was evaluated in non-aqueous electrolyte using dilute HCl (0.1–0.4 N), acetic acid (AcOH) (0.1–1 M, pH 2.4 to 2.9), *p*-toluene sulphonic acid (PTSA) (0.1–0.5 N), and sulphate buffer (MeCN : buffer:: 9 : 1–9 : 2, pH 2) as the proton sources. A comparison of the HER performance of carbon-based nanomaterials, *i.e.*, metal-free electrocatalysts, suggests the superior efficacy of *h-OLF* with respect to other catalysts, as summarized in Table 1.

Sagarika Bhattacharya

Dr. Sagarika Bhattacharya is an Assistant Professor at the Department of Chemistry, National Institute of Technology Raipur (NIT Raipur), India. She has received B.Sc., M.Sc., and Ph.D. in Chemistry from University of Calcutta, India. After the doctoral studies she spent three and half years at Ben Gurion University of the Negev, Israel as a postdoctoral researcher. Her research group is currently interested in synthesizing metal free fluorescent carbon nanoparticles in bottom-up technique for biological and multimodal applications. Additionally, Bhattacharya research group is also engaged in exploring the fascinating fluorescence of lanthanides, aiming to achieve pure white light.

Experimental section

Materials

Glucose, sulphanilamide, ethanol, and H_2SO_4 (98%) were purchased from CDH. Dialysis tubing membrane (2000 MWCO), KBr, HCl (38%, Actylis), AcOH (99.8%, Qualigens), PTSA (98%, TCI), MeCN (99.8%, Finar), tetrabutylammonium perchlorate (TBAP) (99%, Alfa Aesar) and KOH (99.9%, Qualigens) were used in the experiments.

Synthesis of glucose–sulphanilamide hollow Onion-Like Fullerenes (*h-OLF*s)

Hollow-Onion-Like Fullerenes (*h-OLF*s) were synthesized from glucose and sulphanilamide in a ratio of 2 : 1 (mM concentration) in 40% ethanol–water solution. The abovementioned mixture was placed in a Teflon liner inside a hydrothermal

chamber and kept in a hot air oven at 180 °C for 6 hours. After the completion of the reaction, the chamber was allowed to cool down to room temperature. The *h-OLF* solution was centrifuged at 10 000 rpm for 10 minutes to precipitate out unreacted/heavy particles. The supernatant solution was subjected to dialysis in deionized water for 3 days. After dialysis, the *h-OLF* solution was dried at 60 °C and used in subsequent characterization studies and electrocatalytic HER applications.

Characterization

Fluorescence spectroscopy. The fluorescence emission spectra of *h-OLF* (1 mg mL^{-1}) were recorded upon excitation within a range of 300–500 nm at 25 nm intervals, using a Hitachi F-4700 fluorescence spectrophotometer equipped with a 150 W xenon lamp. The photostability experiments were carried out with continuous UV exposure of 365 nm UV light for 3 hours. On the other hand, the effect of pH on fluorescence intensity was measured by varying pH values from 3 to 12. Additionally, the photo-thermal stability of *h-OLF* was recorded by changing the temperature from 10 to 60 °C.

Fourier transform infrared (FT-IR) spectroscopy. The FT-IR spectra were recorded using a Bruker Alpha spectrometer over the spectral range of 4000–400 cm^{-1}. KBr pellets of dried *h-OLF* samples were prepared for measurement.

Raman spectroscopy. Raman spectroscopy of *h-OLF* was performed using a Research India RIAR-0403 Raman spectrometer. A dried sample of *h-OLF* was used for the experiment.

Ultraviolet–visible (UV–vis) spectroscopy. An Agilent Cary 60 UV-vis spectrophotometer was used to record the absorption spectra of *h-OLF*. Agilent quartz cells with a path length of 1 cm and a total cell volume of 3 mL were used to collect the UV data. A dilute solution of *h-OLF* prepared in water was used when performing the UV-vis experiment.

Powder X-ray diffraction (XRD). Powder XRD patterns were recorded using a PANalytical 3 kW X'pert Powder multifunctional diffractometer over the 2θ range of 10 to 40°.

High-resolution transmission electron microscopy (HR-TEM). A Tecnai 200 kV G2 20 S-TWIN [FEI] microscope was used for capturing HR-TEM images. The sample was prepared by drop-casting on a graphene-coated copper grid.

pH measurement. The pH measurement was performed using an Eutech pH meter. Solutions of *h-OLF* (1 mg mL^{-1}) from pH 3 to pH 12 were prepared at room temperature by the simultaneous addition of acid (HCl, 0.1 N) and base (NaOH, 0.1 M).

X-ray photoelectron spectroscopy (XPS). The *h-OLF* sample for XPS analysis was prepared by drop-casting the *h-OLF* solution onto silicon wafers and drying these on a hot plate to create a layer of sample on their surface. For XPS data analysis, CASA (XPS software), Electron Spectroscopy for Chemical Analysis (ESCA), and Omicron Nanotechnology features were used. A characteristic energy of 1486.7 eV was employed in all XPS measurements. The acquisition time for survey and C 1s spectra was 0.1 s, and for other high-resolution energy spectra, the acquisition time was 0.15 s.

Zeta potential. The surface charge of *h-OLF* was measured using an Anton Paar Litesizer 500 zeta potential analyzer. The experiments were performed with a 1 mg mL^{-1} aqueous solution of *h-OLF*, while varying the pH value from 3 to 12.

Scanning electron microscopy-energy dispersive X-ray spectroscopy (SEM-EDX). The surface mapping of constituent elements and elemental % analysis of the as-synthesized *h-OLF* sample and the sample deposited on the NF electrode after the CA-HER was performed using a Hitachi Flex SEM 1000 II instrument.

Catalyst ink preparation and electrode surface deposition. 3D porous nickel foam (NF) of 0.5 cm thickness was selected as the electrode substrate for the deposition of the catalyst. The NF sheet was cut into pieces of 1 × 2 cm^2 and these pieces were ultrasonically washed with 0.1 N HCl for 10 minutes. According to our previous studies, it was found that the NF surface was stable for up to 20 minutes in 0.1 N HCl before it starts forming a thin amorphous layer of NiO.[47] Subsequently, the NF pieces were twice washed with Milli-Q water and once with acetone for 10 minutes each. The electrode substrates were then dried in an oven set at 50 °C overnight. Catalyst ink was prepared using Nafion and ethanol as the dispersion medium. A 1.0 wt% Nafion solution in ethanol was diluted, and the *h-OLF* solution was added. The mixture was sonicated for 10 minutes at room temperature to ensure homogeneity. The resulting catalytic ink was pipetted and dropwise deposited onto the pre-washed NF surface, coating a 1 × 1 cm^2 area of the electrode. The coated electrodes were dried overnight at room temperature, with a catalyst loading of 5 mg per NF substrate for subsequent electrochemical studies.

Preparation of electrolytes. To study the HER, acetonitrile (ACN) was chosen as a non-aqueous medium, and 0.5 M tetrabutylammonium perchlorate (TBAP) was added as a supporting electrolyte.

A 0.05 M sulfate buffer (HSO_4^-/SO_4^{2-}) at pH ~ 1.9 was prepared using Na_2SO_4 and $NaHSO_4$ in water. The amount of Na_2SO_4 and $NaHSO_4$ used to make the 0.05 M buffer was calculated using the following equation:

$$pH = pK_a + \log[SO_4^{2-}]/[HSO_4^-] \quad \text{(i)}$$

Different ratios of sulphate buffer and non-aqueous electrolyte (0.5 M in acetonitrile (ACN)) were used to perform the electrolysis.

Different concentrations of AcOH, HCl and PTSA were prepared by mixing the desired amount of glacial acetic acid (17.4 M), HCl (11.6 M), and PTSA, respectively, with the non-aqueous electrolyte of 0.5 M TBAP in ACN.

Electrochemical measurements. A potentiostat/galvanostat (Metrohm Autolab, serial no. MAC90835) instrument was employed for electrochemical measurements, and the obtained data were analyzed using Origin software. A three-electrode system was used for the electrochemical studies. The NF loaded with catalytic ink is the working electrode (WE), a graphite rod (diameter = 2 mm) is used as the counter electrode (CE), and Ag/AgCl (3.5 M KCl, E_0 = 0.205 V *vs.* SHE) is

used as the reference electrode. The electrodes were placed at a distance of ~0.5 cm in all experiments. Using the ACN, electrolytes of different pH based on dilute HCl (0.1–0.4 N; pH 0.4–1), acetic acid (AcOH) (0.1–1 M; pH 2.4–2.9), *p*-toluene sulphonic acid (PTSA, organic acid) (0.1–0.5 N), and sulphate buffer (MeCN : buffer, 9 : 1–9 : 2, pH 2) were prepared. Furthermore, the mixture of sulphate buffer (pH 1.97) and MeCN was also used as an electrolyte to perform the electrocatalytic HER. A constant electrolyte volume of 20 mL was maintained in all experiments to ensure comparability across different electrolytes. Linear sweep voltammetry (LSV) was performed to study the electrochemical HER activity. The following relationship was applied to the conversion of the potential of the reference electrode with respect to the potential of the reversible hydrogen electrode (RHE):[47]

$$E(\mathrm{RHE}) = E^{\circ}_{(\mathrm{ref.})} + 0.098\,\mathrm{V} + (0.059 \times \mathrm{pH})\,\mathrm{V} \quad \text{(ii)}$$

HER activity was studied at a scan rate of 1 mV s^{-1} over a potential range of +0.4 to −0.8 V (*vs.* RHE). At a particular current density, the overpotential (η) was calculated from the obtained polarographs. The Tafel slope was obtained from the linear region of the η *vs.* log$j$ plot, according to the Tafel eqn (iii):[48]

$$\eta = b \log j + a \quad \text{(iii)}$$

where η represents the overpotential (mV), b is the Tafel slope (mV dec^{-1}), and log$j$ is the current density (mA cm^{-2}). The term a refers to the intercept when log$j$ = 0.

The surface area of the catalyst taking part in the catalytic activity was determined using the ECSA (electrochemically active surface area). The ECSA was measured from the double layer capacitance (C_{dl}) of the catalyst. In the non-faradaic region of 0.8953 V–0.9953 V *vs.* RHE, CV analysis on each catalyst was performed at scan rates of 10, 25, 50, 100, 150, and 200 mVs^{-1} to determine the C_{dl} (double layer capacitance). From the plot of the charging current (at the midway potential of each redox half of the CV curve) against the scan rate, a linear slope of the C_{dl} at the electrode–electrolyte interface was obtained.[49] Eqn (iv) was then applied to calculate the ECSA:[48]

$$\mathrm{ECSA} = C_{dl}/C_s \quad \text{(iv)}$$

where C_s is the specific capacitance of the material under identical electrolytic conditions. The C_s value for NF is considered to be 1.7 mF cm^{-2}.[50] In the frequency region of 100 mHz–1 MHz, EIS (electrochemical impedance spectroscopy) was performed at a constant potential of −0.5 V (*vs.* RHE) for impedance measurements in all the electrolyte media since at this potential, appreciable catalytic activity was observed in all cases. The collected data were plotted as Re(Z) (real part of the impedance) *vs.* Im(Z) (imaginary part of the impedance) to obtain a semicircular Nyquist plot, which was further fitted to an equivalent RC circuit model using Nova software (Metrohm Autolab). To evaluate the long-term stability of the catalyst toward the HER, chronoamperometric (CA) measurements were performed at −0.2 V *vs.* RHE, a potential that corresponds to ~20 mA cm^{-2} in the HER-LSV curves (Fig. 7d).

Results and discussion

In this study, hollow Onion-Like Fullerenes were prepared hydrothermally with a 2 : 1 ratio of glucose and sulphanilamide in water–ethanol mixture at 180 °C for 6 hours, as illustrated in Scheme 1. The synthesized *h-OLF* and its HER activity are shown in Fig. 1(a and b). According to a general description of the functional group-modified *h-OLF*-type materials, the graphitic core of *h-OLF* is comprised of carbonized glucose, while the sulphanilamide fragments are retained on the surface of the carbon nanoparticles due to the application of lower temperatures. Multiple spectroanalytical techniques were employed to characterize the as-synthesized functional group-modified *h-OLF*. The UV-visible spectra of *h-OLF* show two bands at 262 nm and 342 nm, as shown in Fig. 2(a). The peak at 262 nm corresponds to $\pi \rightarrow \pi^*$ transitions of aromatic and graphitic C=C, while the shoulder at 342 nm represents $n \rightarrow \pi^*$ symmetrically forbidden electronic transitions of C=O and S=O originating from glucose and sulphanilamide molecules.[51] Previous reports confirm the retention of the molecular fragments on the surface of the carbon nanoparticles due to the use of mild conditions.[51,52] Various spectroscopic techniques identified the retained moieties on the surface of the carbon nanoparticles.

In the FT-IR spectrum, stretching frequencies of the alcoholic O–H bond of glucose and –NH_2 from sulfanilamide were positioned at 3431 cm^{-1} and 3181 cm^{-1}, respectively.[51] The FT-IR peak positioned at 2852 cm^{-1} shows the symmetric

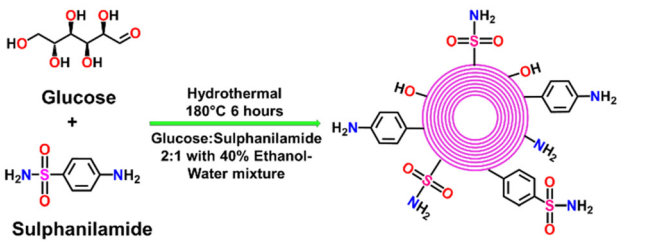

Scheme 1 Scheme representing the synthesis of hollow Onion-Like Fullerene ring (*h-OLFs*).

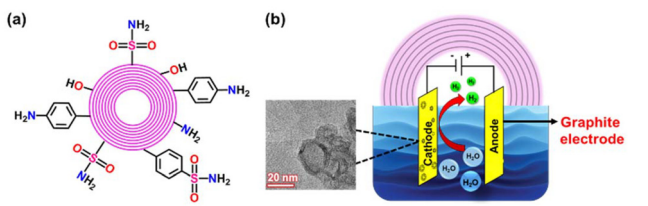

Fig. 1 The *h-OLF* material and its application. (a) Schematic representation of the carbon nanomaterial and (b) HER activity; inset: HR-TEM image.

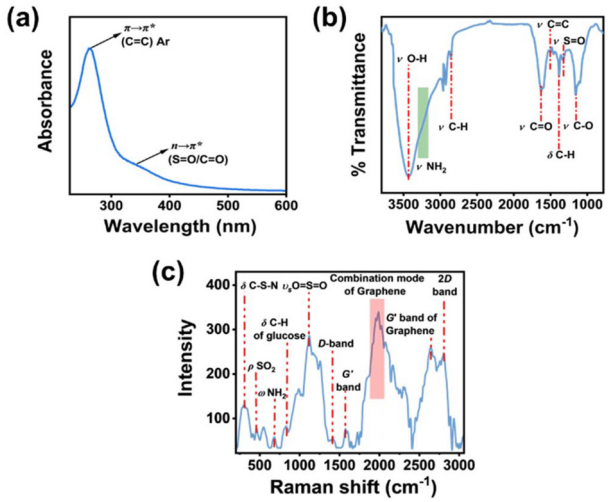

Fig. 2 Spectroscopic characterizations of *h-OLF*. (a) UV-vis, (b) FT-IR, and (c) Raman spectra.

stretching of sp^3 –C–H.[53] The peaks at 1628 cm^{-1}, and 1460 cm^{-1} correspond to the stretching modes of C═O and C═C.[51,54,55] The S═O bond of sulfanilamide was identified at 1330 cm^{-1}, and the low intensity peaks at 1384 cm^{-1}, 1157 cm^{-1}, and 1126 cm^{-1} are attributed to the stretching vibrations of C–H, C–O, and C–S, as shown in Fig. 2(b).[51,56,57] Analysis of the Raman spectra, as shown in Fig. 2(c), reveals the peaks assigned as follows: (i) 300 cm^{-1} for the torsion of $–NH_2$ or the deformation of C–S–N; (ii) 450 cm^{-1} for the rocking of $–SO_2$; (iii) 680 cm^{-1} for the wedging of $–NH_2$;[58] (iv) 893 cm^{-1} for the deformation of C–H in glucose;[59] (v) 1130 cm^{-1} for the symmetric stretching of $–SO_2$;[58] (vi) 2000 cm^{-1} for the combination mode of graphene; (vii) 2521 cm^{-1} for the G′ band of graphene;[60] and (viii) 2805 cm^{-1} for the 2D band.[61]

The use of X-ray photoelectron spectroscopy (XPS) once again verifies the conservation of the functional group originating from the molecular precursors. The survey spectra of *h-OLF* shows the presence of C, O, N, and S elements in the *h-OLF*, as shown in Fig. 3(a). The deconvoluted XPS spectra of C 1s confirm the presence of five different types of carbon-containing moieties and are attributed to sp^2 C═C (284.2 eV), with small peaks at 284.6 eV, 285.2 eV, and 288.7 eV attributed to sp^2 carbon atoms, C═C, C–N/C–S, and C═O, respectively, as shown in Fig. 3(b).[51,62] The O 1s spectra of *h-OLF* can be deconvoluted into three peaks at 530 eV, 531.5 eV, and 532 eV, corresponding to C–OH, S═O, and C═O, respectively, as shown in Fig. 3(c).[52,63,64] The S 2p spectra of *h-OLF* reveals two peaks at 169 eV and 170 eV, which are assigned to S═O and S–N/S–C groups, as shown in Fig. 3(d). The deconvoluted peaks of N 1s with two different types of nitrogen species at 399.1 eV and 399.9 eV are attributed to C–N/S–N and N–H bonds, respectively, as shown in Fig. 3(e).

The percentage composition of C 1s was 4.12%, S 2p was 5.27%, N 1s was 0.48%, and O 1s was 1.91%. The composition and elemental ratio of the constituent elements on the surface of the synthesized *h-OLF* were subsequently studied through the SEM-EDX mapping technique. The electrocatalyst, *i.e.*, the *h-OLF*, was deposited on the Ni foam for the preparation of the electrode. Fig. 4(a) shows the FE-SEM image of the catalyst-coated Ni foam and the homogeneous distribution of C, O, S, and N on the surface of *h-OLF* (Fig. 4b–d). The EDX mapping study (Fig. S1 and Table S1) of *h-OLF* confirmed the presence of C, O, S, and N elements with atomic ratios of 59.47%, 34.88%, 3.35% and 2.31%, respectively, indicating the integrity of the Ni foam electrode after deposition of the carbon nanomaterial. From the FE-SEM image, the presence of a mixture of aggregated spherical and rod-shaped particles could be seen. The crystalline nature of *h-OLF* was identified using the XRD technique, where three reflection planes of (002), (111), and (110) (JCPDS no. 03-0884) were observed at 2θ values of 20.8°, 29.0°, and 31.8°.[65] The XRD peaks between 23° and 27° corresponds to the sp^2 carbon present in the *h-OLF*. These peaks can be ascribed to various forms of carbon including turbostratic carbon and graphitic carbon whose reflection plane is represented as (001).[66,67]

The *d*-spacing values of *h-OLF* were 0.44 and 0.21 nm, which could be indexed to the (002) and (110) graphitic crystal planes, respectively, as shown in Fig. 5(a).[51,52,58] The HR-TEM images in Fig. 5(b) revealed the formation of multiple con-

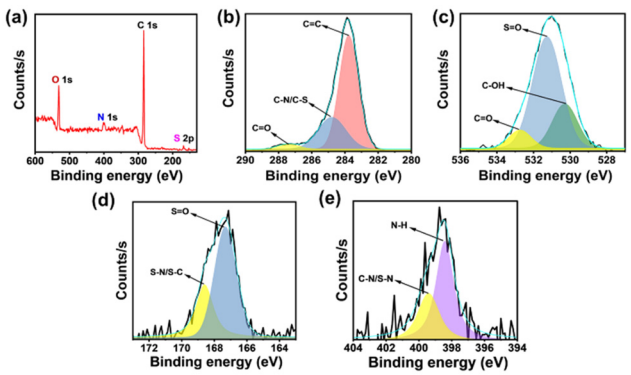

Fig. 3 XPS analysis of *h-OLF*. Deconvoluted spectra of the core-level. (a) XPS survey spectrum and (b) C 1s, (c) O 1s, (d) S 2p, and (e) N 1s XPS spectra.

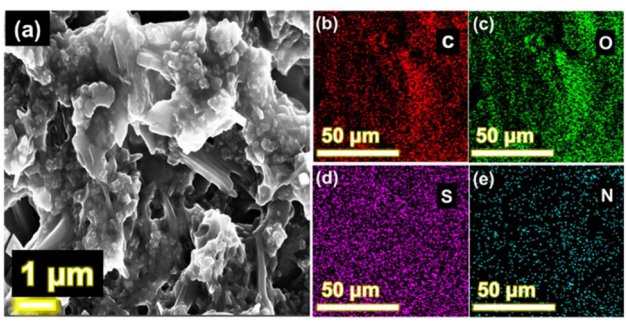

Fig. 4 FE-SEM image of *h-OLF*. (a) Deposited *h-OLF* on NF and (b–e) SEM-EDX elemental mapping of the selected region of the sample displaying the distribution of (b) C, (c) O, (d) S, and (e) N.

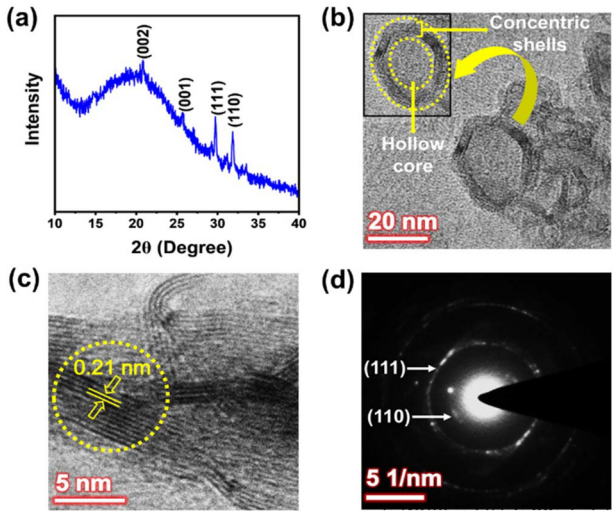

Fig. 5 Characterization of *h-OLF*. (a) Powder XRD pattern, (b) High-resolution transmission electron microscopy (HR-TEM) images, (c) Well-resolved lattice fringes with a *d*-spacing of 0.21 nm, and (d) SAED pattern.

centric layers and could be assigned to the *h-OLF*. Well-resolved lattice planes were noted with an interplanar distance of 0.21 nm, corresponding to the (110) plane of graphite, as shown in Fig. 5(c). The SAED pattern represents the crystalline nature of the material with *d*-spacing values of 0.30 and 0.21 nm, assigned to the (111) and (110) graphitic planes, as shown in Fig. 5(d). The *h-OLF* was found to be polycrystalline as evidenced by the SAED and powder XRD patterns.[52,68] The fluorescence properties of *h-OLF* under different conditions were studied with a 1 mg mL^{-1} solution. To determine the photostability of the newly synthesized carbon onion ring, the excitation-dependent emission spectra were recorded by varying the excitation wavelength from 300 to 500 nm with defined intervals of 25 nm. The maximum emission was observed at 457 nm upon excitation at a wavelength of 375 nm, as shown in Fig. 6(a). The fluorescence excitation and emission spectra of *h-OLF* were recorded and are presented in Fig. 6(b). The photostability of the *h-OLF* rings was identified by varying the temperature (10–60 °C), as shown in Fig. 6(c).

The *h-OLF* rings can efficiently resist the bleaching of emission intensity upon irradiation with 365 nm UV light even over long exposure times of 3 hours, as shown in Fig. 6(d). The pH-dependent fluorescence emission of *h-OLF* was examined to assess its proton absorption capacity, given that hydrogen evolution is inherently a pH-dependent process. A sudden increase in FL emission was noticed due to the protonation of $-NH_2$, while after pH 10, it decreased due to the deprotonation of –OH, as shown in Fig. 6(e). Previously, for citric acid/sulfanilamide carbon dots, the aggregation-induced quenching of photoluminescence was reported for very low (<2) and high pH (>12), as evidenced from DLS (dynamic light scattering).[51] Hence, zeta potential measurement of *h-OLF* was carried out at different pH values from 3 to 12. When reducing the pH from 12 to 2, the amino groups originating from the sulphanilamide present on the *h-OLF* surface were protonated, as evidenced from the zeta potential *vs*. pH plot, as shown in Fig. 6(f).

Electrocatalytic HER study with the *h-OLF*

The *h-OLF* catalyst (3.5 mg) was deposited on nickel foam of 1 cm^2 surface area (*h-OLF*/NF) and was used as the working electrode in a three-electrode cell set-up including a graphite rod as the counter electrode, while Ag/AgCl (3.5 M KCl) was used as the reference electrode, in order to conduct electrocatalytic experiments. To investigate the HER activity of *h-OLF*, a non-aqueous medium was preferred. TBAP (0.05 M) in acetonitrile was chosen as the electrolyte into which different organic or inorganic acids were added in measured quantities. At first, in the electrolyte, different amounts of *p*-toluene sulphonic acid (PTSA) were added to test the HER activity. PTSA is a strong organic acid, fully dissociating in aqueous or mixed aqueous–organic media, effectively acting as a proton source for the HER. Increasing PTSA concentration increases the proton activity, which enhances the HER kinetics. Cyclic voltammetry (CV) and linear sweep voltammetry (LSV) were performed within a potential range of +0.4 to −0.8 V (*vs.* RHE). The CV cycles were recorded to observe the changes in the limiting current density in each cycle, possibly due to the activation of the catalyst. In the optimized electrolyte system, *i.e.*, 0.3 N HCl, it was observed that there was minimal change in the limiting current throughout 10 CV cycles, signifying the minimal effect of CV activation on the catalyst's activity (Fig. S2). Hence, the LSV study was performed in all electrolyte media without prior activation, and the real activity of the as-synthesized material was reported. Moreover, the catalyst loading was optimized in 0.3 N HCl.

It was observed that for 1 and 2.5 mg loadings, the catalyst achieved only 50 mA cm^{-2} current density. Upon increasing the loading to 3.5 and 4 mg, the catalytic current density greatly increased (Fig. S3). However, in the case of 4 mg loading, although the current density increases slightly when compared to 3.5 mg loading, the onset potential was more positive, and the kinetic region showed reduced current density at higher potentials. Therefore, 3.5 mg was chosen as the optimal loading for all electrochemical experiments. With increasing concentration of PTSA in the electrolyte, there was a gradual and exponential enhancement in the cathodic current density beyond −0.2 V (*vs.* RHE). The increase in the current density was found to be optimum when 0.5 M PTSA was present in the electrolyte.

At an applied potential of −0.4 V, a cathodic current density of 1 mA cm^{-2} was achieved, which indicates the reduction of freely available protons to hydrogen, as shown in Fig. 7(a). To improve HER activity, in a similar three-electrode setup, 0.05 M sulphate buffer at pH 1.9 was added to the non-aqueous electrolyte, and LSV studies were conducted. From the LSV curves recorded in the non-aqueous electrolyte with various buffer contents, a slow enhancement of the catalytic current density was observed, and to reach a cathodic current density of 1 mA cm^{-2}, an applied potential of −0.2 V was required

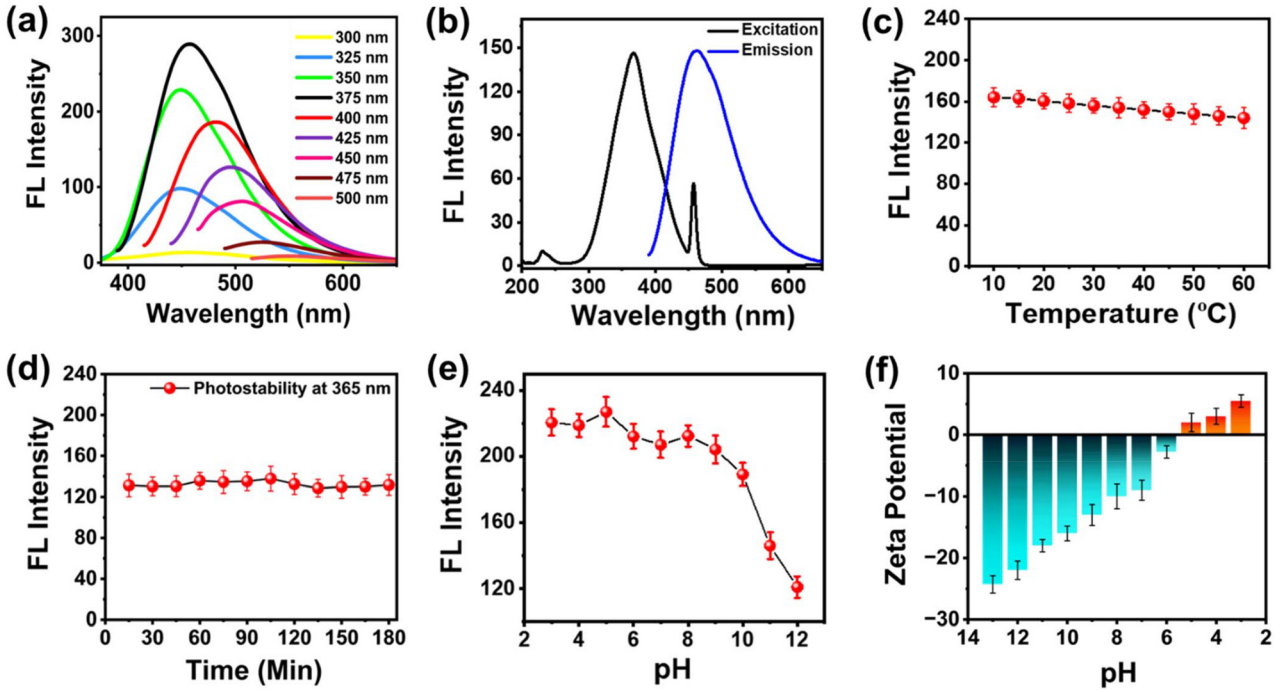

Fig. 6 Fluorescence spectra and stability study of *h-OLF*. (a) Fluorescence spectra, (b) Fluorescence emission and excitation spectra, (c) Fluorescence stability at different temperatures, (d) Fluorescence stability under exposure of 365 nm UV light, (e) Effect of pH on fluorescence, and (f) Zeta potential at various pH values.

(Fig. S4). Addition of 2 mL of 0.05 M sulfate buffer to 8 mL of ACN (with 0.05 M TBAP) leads to an optimum cathodic current density of 2 mA cm^{-2} at −0.45 V *vs.* RHE. Despite the high capacitive current in the low-potential region, the improvement of catalytic current density upon the addition of the sulfate buffer to the non-aqueous medium resulted in increased proton availability, with the nearly two-fold enhancement of the cathodic current density (at a fixed potential) indicating improved HER performance. Next, acetic acid (AcOH), a weak organic acid, was used as the proton source in the non-aqueous electrolyte. In a similar electrochemical setup, the addition of different concentrations of AcOH to the electrolyte resulted in LSV polarization curves showing notable improvements in the cathodic current density with increasing concentration of AcOH, as shown in Fig. 7(b). At low AcOH concentrations of 0.1–0.3 M, the cathodic current density reached a limiting value by −0.4 V, whereas on increasing the AcOH concentration in the electrolyte to 1 M, the catalytic current density was observed after −0.1 V *vs.* RHE. Notably, j_c values of 1 mA cm^{-2} and 2 mA cm^{-2} can be achieved with applied potentials of −0.1 V and −0.19 V, respectively. However, the highest HER activity was observed with 0.9 M AcOH, where LSV studies revealed exponential current growth after −0.3 V, reflecting enhanced catalytic proton reduction during the HER.However, on increasing the concentration of AcOH beyond 0.9 M, the sulphanilamide groups on the surface of *h-OLF* can strongly interact with acetate ions *via* hydrogen bonding and electrostatic forces, potentially leading to adsorption and blockage of active sites on the catalyst, resulting in decreased HER activity at higher acetate concentrations.[69] Notably, the activity of the catalyst was significantly improved in the presence of AcOH in comparison with *p*-TsOH or the addition of buffer. The rate of the HER can be experimentally verified by altering the concentration of the proton source in the electrolyte.[70] Hence, the order of the reaction with respect to [AcOH] was derived from the LSV curves of variable concentrations of AcOH. The variation in the *j* value (at −0.1 V) can be correlated to the acid concentration, where a linear slope between log*j* *versus* log[AcOH] (@−0.1 V *vs.* RHE) represents a first order dependence of the rate of the HER with respect to [AcOH], as shown in Fig. 7(c), which implicates proton adsorption-mediated HER activity.

However, AcOH is a weak acid with a pK_a value of ∼3 with a low dissociation constant, for which the catalytic current density hardly reaches 8 mA cm^{-2} at a terminal cathodic potential of −0.78 V. To achieve improved activity, a Brønsted acid with a high dissociation constant, such as dilute HCl, was used as the proton source. The LSV studies performed using a similar electrochemical setup, where *h-OLF*/NF was used as the cathode and a dilute HCl solution was gradually added to the non-aqueous electrolyte, revealed remarkable improvement in HER activity. Upon addition of 0.1 N HCl to the electrolyte, an almost 2–3-fold enhancement of the cathodic current density over the entire cathodic region was seen for the *h-OLF*/NF compared to bare NF. It was subsequently observed that with 0.3–0.4 N HCl present in the ACN electrolyte, the highest HER

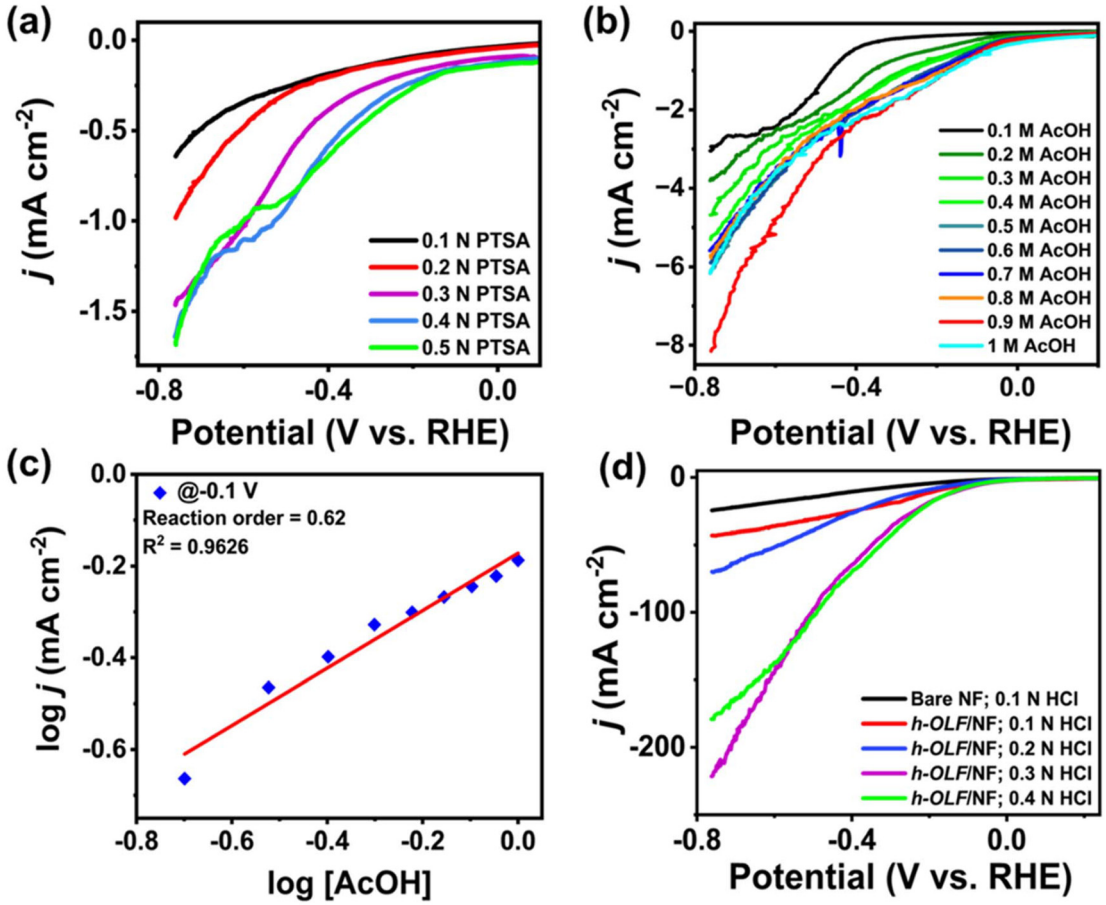

Fig. 7 Electrochemical experiment. (a) Concentration-dependent LSV polarization curves for the HER with *h-OLF*/NF in MeCN (containing 0.05 M TBAP) solution in the presence of different amounts of PTSA, (b) AcOH as the proton source. (c) Correlation of log*j vs.* log[AcOH] and order of the reaction with respect to [AcOH]. (d) LSV polarization curves in MeCN (containing 0.05 M TBAP) solution after the addition of dilute HCl. LSV curves are non-*iR* corrected and the scan rate is 1 mV s^{-1}.

efficiency was achieved. From the LSV curves shown in Fig. 7(d), it is noted that only at an applied potential of −133 mV, is a high catalytic current density of −10 mA cm^{-2} achieved. Moreover, at potentials of −0.43 V and −0.64 V (*vs.* RHE), the *j* values reached 100 mA cm^{-2} and 200 mA cm^{-2}, respectively. In the case of the HER in acetonitrile with 0.1 N HCl, the overpotential (η) of *h-OLF*/NF was 219 mV while that for bare NF was 383 mV, highlighting the active participation of the *h-OLF* catalyst in the HER. The catalyst activity constantly increased up to 0.4 N HCl with a very small overpotential of 133 mV. In contrast, using weak acids, *i.e.*, acetic acid, *p*-toluene sulphonic acid, and sulphate buffer, the activity of the catalyst was inferior to that when using HCl, plausibly due to their limited dissociation when fewer protons are available in the electrolyte (Fig. S5). It is evident from the acid-concentration study in acetonitrile that 0.1–0.4 N HCl provides the best conditions to study the HER. With an increase in the acidity, *i.e.*, the HCl concentration, the number of protons increased, which in turn augmented the catalyst's activity towards the electrochemical HER. However, the activity of Pt far surpasses the activity of *h-OLF* (Fig. S6). The electrokinetics of the HER in various acid-containing non-aqueous electrolytes was subsequently evaluated by performing Tafel analysis. In acidic media, the formation of [$*H_{ads}$] species from the free $[H_3O]^+$ accelerates as a function of acid strength, which enhances the HER activity of the catalyst.[71,72] The Tafel slopes obtained from the LSV curves show a trend similar to that of the HER activity. The Tafel slope for the *h-OLF*/NF in 0.4 N HCl was 251 mV dec^{-1}, the lowest among all values recorded. Due to the higher dissociation of HCl (a Brønsted acid), compared to weaker acids like AcOH or *p*-TsOH, which remain largely undissociated, dilute HCl-containing electrolytes show faster electrokinetics, as shown in Fig. 8(a).[73] Despite superior catalytic current density at high HCl concentration, surface poisoning of the catalyst by Cl^- has been reported in strong HCl solutions.[74] Therefore, the 0.1 N HCl-containing electrolyte was chosen for the EIS study. The Nyquist plots were obtained from the EIS study, and from the semicircular arcs of the plots, the lowest charge transfer resistance (R_{ct}: 12.18 Ohm) was observed with the *h-OLF*/NF in 0.1 N HCl electrolyte among other acid electrolytes of the same strength, as shown in Fig. 8(b). Additionally, the Nyquist curves of *h-OLF*/NF in

different electrolyte media and corresponding circuit fitting are shown in Fig. S7. The observed R_{ct} values based on the fitted impedance data for other electrolytes follow the same trend as the HER activity trend in different acid-containing electrolytes, *i.e.*, 0.1 N HCl < 0.1 N AcOH < 9 : 2 ratio of 0.05 M TBAP in MeCN and sulphate buffer < 0.1 N PTSA < 0.05 M TBAP in MeCN with respective R_{ct} values of 12.18, 194.9, 368.87, 639.71, and 1572.35 Ohm, as shown in Fig. 8(c). In the case of the HER in HCl-containing electrolytes, the higher activity can also be explained by the greater availability of substrate and more involvement of the active sites during the HER. The C_{dl} value of *h-OLF*/NF was calculated from the CV cycles in the non-faradaic region in the presence of different acid-containing electrolytes of the same strength, as shown in Fig. 8(d) and Fig. S8. The C_{dl} value of *h-OLF*/NF was 0.22 mF cm^{-2} in the 0.1 N HCl-containing electrolyte, which corresponds to an electrochemical surface area of ~0.13 cm^2, and this value is the highest among all the values obtained in different acid-containing electrolytes. These data justify the participation of the maximum number of surface sites of the *h-OLF* during the HER, thus imparting the highest catalytic current density and the highest HER activity. Therefore, the highest HER activity of *h-OLF*/NF was noted in the dilute HCl-containing electrolyte. Furthermore, 0.1 N HCl-containing electrolyte was used to perform the bulk electrolysis for a prolonged period.

Chronoamperometry (CA) was performed at a fixed potential of −0.2 V (*vs.* RHE). At the beginning of the CA study, the $j_{cathode}$ value was 22.5 mA cm^{-2}, which gradually decreased to 15 mA cm^{-2} over a period of 5000 s due to the rapid consumption of H^+ from the electrolyte (Fig. S8). However, the activity of the catalyst, *i.e.*, $j_{cathode}$, can be restored by periodic addition of further dilute HCl to maintain a concentration of 0.1 N HCl. A plausible mechanism of the HER performance using the carbon-based *h-OLF* catalyst is shown in Fig. 9. The CA analysis was continued over several cycles of 5000 s each, and each step was accompanied by the addition of HCl to the electrolyte,

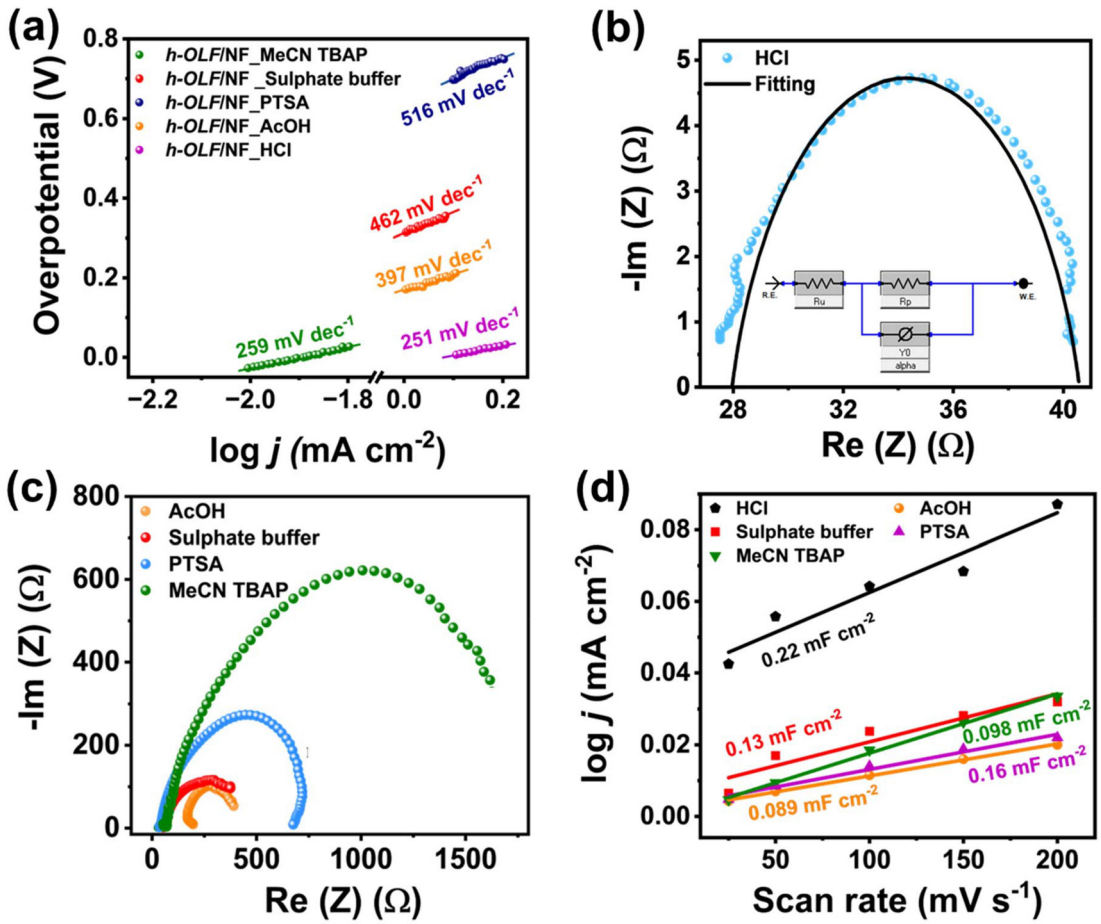

Fig. 8 Electrochemical experiment. (a) Tafel slope obtained with *h-OLF*/NF in MeCN (containing 0.05 M TBAP) solution in the presence of 0.1 N HCl, 0.1 M AcOH, a 9 : 2 ratio of 0.05 M TBAP in MeCN and sulphate buffer, 0.1 M PTSA and 0.05 M TBAP in MeCN. (b) Nyquist plot of *h-OLF*/NF in MeCN (containing 0.05 M TBAP) solution in the presence of 0.1 N HCl (inset: parallel RC circuit fitting). (c) Nyquist plot obtained from electrochemical impedance spectroscopy (EIS) in 0.1 M AcOH, a 9 : 2 ratio of 0.05 M TBAP in MeCN and sulphate buffer, 0.1 M PTSA and 0.05 M TBAP in MeCN (inset: parallel RC circuit fitting; in the equivalent circuit fitting, R_u is the solvent resistance, $R_p = R_{ct}$ is the charge transfer resistance and $C_f = C_{dl}$ is the double layer capacitance). (d) The C_{dl} values obtained for *h-OLF*/NF in MeCN (containing 0.05 M TBAP) solution in the presence of 0.1 N HCl, 0.1 M AcOH, a 9 : 2 ratio of 0.05 M TBAP in MeCN and sulphate buffer, 0.1 M PTSA and 0.05 M TBAP in MeCN.

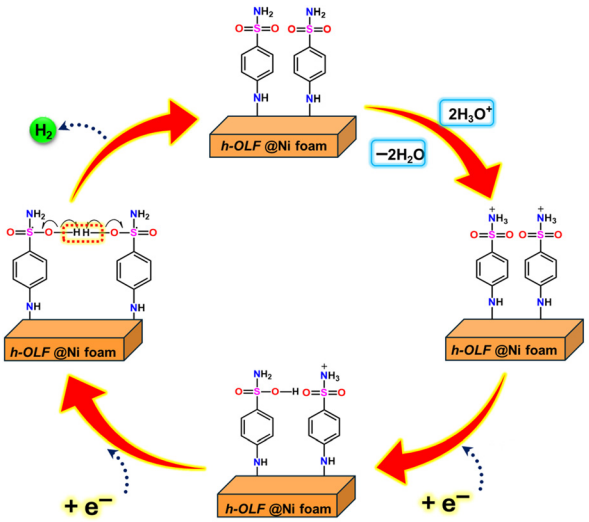

Fig. 9 Plausible mechanism of HER performance by the *h-OLF*.

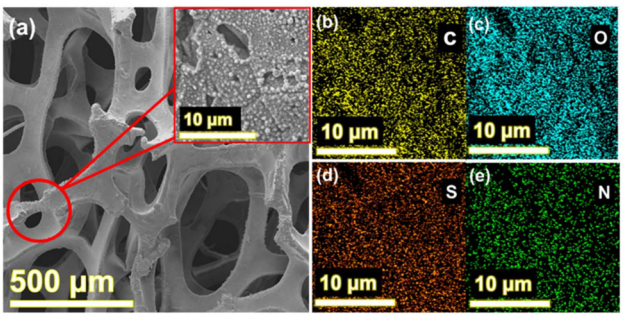

Fig. 10 Post-catalytic characterization. (a) FE-SEM image of the *h-OLF* catalyst on NF after electrocatalysis and (b–e) SEM-EDX elemental mapping showing the distribution of (b) C, (c) O, (d) S and (e) N on *h-OLF*/NF.

maintaining a constant supply of protons in the non-aqueous electrolyte. It can be seen that the $j_{cathode}$ value reached 45 mA cm^{-2} after 30 000 s, indicating the superior long-term HER performance of *h-OLF*/NF (Fig. S9). The elemental composition of the used *h-OLF*/NF electrode after electrolysis for 30 000 s in 0.1 N HCl was analyzed by SEM-EDX mapping. It was found that even after electrolysis for 30 000 s, the *h-OLF* material was still retained on the electrode surface, as shown in Fig. 10(a). The respective elements were also uniformly distributed on the surface of the catalyst, as shown in Fig. 10(b–e). After the CA-HER, small alterations in the surface concentration of the elements were evident from the EDX analysis, implying excellent post-catalytic stability of the material even at high proton concentrations (Fig. S10 and Table S2).

Conclusions

Herein, we reported a novel carbon-based material, *h-OLF*, which was prepared *via* a single-step hydrothermal route by using highly abundant and cheap chemicals like glucose and sulphanilamide. This unique hollow nanostructured material with dominant graphitic content enhanced electronic conduction when drop-cast onto a three-dimensional NF surface, exhibiting remarkable HER activity in a mild acid-containing non-aqueous electrolyte. Among previously reported carbon-based materials like C-dots, graphene oxide, *etc.*, *h-OLF* demonstrated excellent electrochemical activity, showing a very low overpotential of 133 mV for the HER. Moreover, the HER activity was investigated with a range of acids, *i.e.*, acetic acid (AcOH), *p*-toluene sulphonic acid (PTSA), sulphate buffer, and HCl, whereupon HCl turned out to be the best proton source due to its stronger dissociation and spontaneous liberation of protons. The facile kinetics of *h-OLF* is the key to its promising HER activity, which will encourage further exploration of its potential in various other electrochemical applications.

Conflicts of interest

The authors declare no conflicts of interest.

Data availability

The data that support the findings of this study are available from the corresponding author upon reasonable request.

Supplementary information (SI): EDX spectra of elements C, N, O, and S present on the surface of the as-synthesized *h-OLF*, percentage elemental composition of elements present on the surface of the as-synthesized *h-OLF*, CV curves in 0.3 N HCl in MECN (containing 0.05 M TBAP) solution. CV curves are non-iR corrected and scan rate 5 mV s^{-1}, concentration-dependent LSV polarization curves for the HER with *h-OLF*/NF (non-*iR* corrected, scan rate: 1 mV s^{-1}) in sulphate buffer in MeCN (0.05 M TBAP) solution, LSV polarization curves with different solvents, The comparative LSV curve of the HER activity of *h-OLF*/NF and Pt, The Nyquist curves of *h-OLF*/NF in different electrolyte media and corresponding circuit fitting. The inset shows the equivalent circuit fitting (R_u = R_s = solvent resistance; R_p = R_{ct} = charge transfer resistance; C_f = C_{dl} = double layer capacitance). ECSA analysis from the CV scans in a non-faradaic potential range of *h-OLF*/NF in MeCN (containing 0.05 M TBAP) solution in the presence of 0.1 N HCl, 0.1 M AcOH, 9 : 2 ratio of 0.05 M TBAP in MeCN and sulphate buffer, 0.1 M PTSA, and 0.05 M TBAP in MeCN. CV cycles were recorded at scan rates of 25 mV s^{-1}, 50 mV s^{-1}, 100 mV s^{-1}, 150 mV s^{-1}, and 200 mV s^{-1}. The chronoamperometry study of *h-OLF*/NF in MeCN (containing 0.05 M TBAP) solution in the presence of 0.1 N HCl. The break in the CA curve indicates the time of addition of HCl to maintain the electrolyte concentration of 0.1 N HCl. EDX spectra of elements C, N, O, and S present on the surface of *h-OLF*/NF after electrocatalysis. Ratio of the elements present on the surface of the catalyst showing a decrease in the concentration of the elements of the functional groups on the surface of *h-OLF*/NF after electrolysis in 0.1 N HCl. Literature survey on previously reported HER

activity of metal-based electrocatalysis and metal-free electrocatalysis. See DOI: https://doi.org/10.1039/d5nr03492b.

Acknowledgements

The authors acknowledge NIT Raipur, the DST-SRG (SRG/2022/000866), and the SEED Grant (NITRR/Seed Grant/2021-22/32) for financial support. I. M. thanks NIT Raipur for providing the Institute Fellowship. I. M. and S. B. also acknowledge the MRC of MNIT Jaipur for the XPS and HR-TEM data.

References

1 S. N. Faisal, E. Haque, N. Noorbehesht, W. Zhang, A. T. Harris, T. L. Church and A. I. Minett, *RSC Adv.*, 2017, **7**, 17950–17958.
2 C. Ray, S. Lee, B. Jin, A. Kundu, J. Park and S. Jun, *ACS Sustainable Chem. Eng.*, 2018, **6**, 6146–6156.
3 S. Paul, S. Sutradhar, A. Paik, A. Biswas, S. Das, C. Das, R. Maity, A. Mahata, S. Midya, B. Maity and S. Rana, *Inorg. Chem.*, 2025, **64**, 7988–8000.
4 A. Paik, C. Das, S. Paul, A. Biswas, S. Mehta, A. Mondal, B. Maity, A. Dutta and S. Rana, *ACS Catal.*, 2024, **14**, 15498–15513.
5 I. O. Cavalcante, F. Neto, P. Sousa, F. Aires, D. Dari, R. Lima and J. S. Dos, *RSC Sustainability*, 2024, **2**, 348–368.
6 M. Cai, L. Xu, J. Guo, X. Yang, X. He and P. Hu, *J. Mater. Chem. A*, 2024, **12**, 592–612.
7 P. Megía, A. Vizcaíno, J. Calles and A. Carrero, *Energy Fuels*, 2021, **35**, 16403–16415.
8 S. S. Dara and D. D. Mishra, *A Text Book of Environmental Chemistry & Pollution Control*, Chand S & Company, 7th edn, 2004.
9 D. Liu, X. Li, S. Chen, H. Yan, C. Wang, C. Wu, Y. A. Haleem, S. Duan, J. Lu, B. Ge, P. Ajayan, Y. Luo, J. Jiang and L. Song, *Nat. Energy*, 2019, **4**, 512–518.
10 L. Fu, X. Zeng, C. Huang, P. Cai, G. Cheng and W. Luo, *Inorg. Chem. Front.*, 2018, **5**, 1121–1125.
11 Y. Li, Y. Sun, Y. Qin, W. Zhang, L. Wang, Mi. Luo, H. Yang and S. Guo, *Adv. Energy Mater.*, 2021, **33**, 17.
12 H. Li and G. Li, *J. Mater. Chem. A*, 2023, **11**, 9383–9400.
13 C. Lim, Z. Sofer, R. Toh, A. Eng, J. Luxa and M. Pumera, *ChemPhysChem*, 2015, **16**, 1898–1905.
14 Y. Gao, Y. Xue, H. Wu, S. Chen, X. Zheng, C. Xing and Y. Li, *J. Am. Chem. Soc.*, 2024, **146**, 10573–10580.
15 M. Kundu, R. Mishra, T. Bhowmik and S. Barman, *J. Mater. Chem. A*, 2018, **6**, 23531–23541.
16 S. Ganguly, P. Basera, S. Ahmed, S. Saha, A. Dutta, C. Loha and S. Ghosh, *Small.*, 2024, **20**, 52.
17 A. Adam, M. Suliman, H. Dafalla, A. Al-Arfaj, M. Siddiqui and M. Qamar, *ACS Sustainable Chem. Eng.*, 2018, **6**, 11414–11423.
18 S. Gupta, M. Patel, A. Miotello and N. Patel, *Adv. Funct. Mater.*, 2019, **30**, 1.
19 Y. Jiang and Y. Lu, *Nanoscale*, 2020, **12**, 9327–9351.
20 X. Xia, L. Wang, N. Sui, V. Colvin and W. Yu, *Nanoscale*, 2020, **12**, 12249–12262.
21 X. Pan, W. He, D. Cao, Y. Li, C. Liu, L. Liang, Q. Hao and H. Liu, *ACS Appl. Nano Mater.*, 2023, **6**, 1724–1731.
22 B. Hou, D. Benito-Alifonso, R. Webster, D. Cherns, M. Galan and J. Fermín, *Catalysts*, 2021, **11**, 681.
23 W. Chen, K. Sasaki, C. Ma, A. Frenkel, N. Marinkovic, J. Muckerman, Y. Zhu and R. Adzic, *Angew. Chem., Int. Ed.*, 2012, **51**, 6131–6135.
24 N. Han, P. Liu, J. Jiang, L. Ai, Z. Shao and S. Liu, *J. Mater. Chem. A*, 2018, **6**, 19912–19933.
25 R. Paul, L. Zhu, H. Chen, J. Qu and L. Dai, *Adv. Mater.*, 2019, **31**, 31.
26 H. Zhong, Q. Zhang, J. Wang, X. Zhang, X. Wei, Z. Wu, K. Li, F. Meng, D. Bao and J. Yan, *ACS Catal.*, 2018, **8**, 3965–3970.
27 F. Besharat, F. Ahmadpoor, Z. Nezafat, M. Nasrollahzadeh, N. Manwar, P. Fornasiero and M. Gawande, *ACS Catal.*, 2022, **12**, 5605–5660.
28 Y. Liu, R. Ali, J. Ma, W. Jiao, L. Yin, C. Mu and X. Jian, *ACS Appl. Energy Mater.*, 2021, **4**, 3861–3868.
29 T. Li, Y. Chen, W. Hu, W. Yuan, Q. Zhao, Y. Yao, B. Zhang, C. Qiu and C. Li, *Nanoscale*, 2021, **13**, 4444–4450.
30 S. Narwade, S. Mali and B. Sathe, *New J. Chem.*, 2021, **45**, 3932–3939.
31 S. Vattikuti, K. C. Devarayapalli, N. Reddy Nallabala, T. Nguyen, N. Nguyen Dang and J. Shim, *J. Phys.Chem. Lett.*, 2021, **12**, 5909–5918.
32 J. Ortiz-Restrepo, O. Loaiza, J. Urresta, J. Velasquez, E. Pastor, M. Chaur and W. Lizcano-Valbuena, *Diamond Relat. Mater.*, 2021, **117**, 108464.
33 V. Rimal, S. Mahapatra and P. Srivastava, *J. Appl. Electrochem.*, 2023, **53**, 285–295.
34 M. Zeiger, N. Jäckel, V. Mochalin and V. Presser, *J. Mater. Chem. A*, 2016, **4**, 3172–3196.
35 S. Sawalha, F. Milano, M. Guascito, S. Bettini, L. Giotta, A. Operamolla, T. Da Ros, M. Prato and L. Valli, *Carbon*, 2020, **167**, 906–917.
36 H. D. Almeida Gonzalez, J. Hernandez Ojeda, A. L. Corcho-Valdés, I. Padron-Ramirez, M. Perez Cruz, C. Iriarte-Mesa, L. F. Desdin-Garcia, P. Gobbo and M. Antuch, *Anal. Sens.*, 2024, **5**, 1.
37 N. Selvaraju, K. Ravichandran and G. Venugopal, *Int. J. Hydrogen Energy*, 2023, **48**, 3807–3823.
38 Y. Liu, N. Ye, X. Li, X. Li, H. Liu, E. Wang, C. Liang and X. Peng, *J. Solid State Chem.*, 2021, **293**, 121781.
39 Y. Zhao, F. Zhao, X. Wang, C. Xu, Z. Zhang, G. Shi and L. Qu, *Angew. Chem., Int. Ed.*, 2014, **53**, 13934–13939.
40 N. Selvaraju, J. Murugan, S. Selvaraj, N. Singhal and G. Venugopal, *Mater. Lett.*, 2023, **341**, 134255.
41 B. R. Sathe, X. Zou and T. Asefa, *Catal. Sci. Technol.*, 2014, **4**, 2023–2030.
42 Y. Tian, R. Mei, D. Xue, X. Zhang and W. Peng, *Electrochim. Acta*, 2016, **219**, 781–789.

43 T. N. Jebakumar I E, R. Atchudan, N. Karthik and Y. R. Lee, *Int. J. Hydrogen Energy*, 2017, **42**, 14390–14399.
44 F. Davodi, M. Tavakkoli, Jo. Lahtinen and T. Kallio, *J. Catal.*, 2017, **353**, 19–27.
45 B. Zhang, H. H. Wang, H. Su, L. B. Lv, T. J. Zhao, J. M. Ge, X. Wei, K. X. Wang, X. H. Li and J. S. Chen, *Nano Res.*, 2016, **9**, 2606–2615.
46 Y. Jiao, Y. Zheng, K. Davey and S. Z. Qiao, *Nat. Energy*, 2016, **1**, 16130.
47 M. K. Adak, H. K. Basak, S. Kumar and B. Chakraborty, *ACS Appl. Nano Mater.*, 2024, **7**, 8329–8340.
48 S. Halder, A. K. Pradhan, S. Khan and C. Chakraborty, *Energy Adv.*, 2023, **2**, 1713–1723.
49 Q. Kang, L. Vernisse, R. C. Remsing, A. C. Thenuwara, S. L. Shumlas, I. G. McKendry, M. L. Klein, E. Borguet, M. J. Zdilla and D. R. Strongin, *J. Am. Chem. Soc.*, 2017, **139**, 1863–1870.
50 C. C. L. McCrory, S. Jung, J. C. Peters and T. F. Jaramillo, *J. Am. Chem. Soc.*, 2013, **135**, 16977–16987.
51 A. Mishra, S. Lzaod, T. Dutta and S. Bhattacharya, *ACS Appl. Bio Mater.*, 2024, **7**, 2752–2761.
52 S. Bhattacharya, R. Sarkar, B. Chakraborty, A. Porgador and R. Jelinek, *ACS Sens.*, 2017, **2**, 1215–1224.
53 Gunture, J. Kaushik, A. Garg, D. Saini, P. Khare and S. Sonkar, *Ind. Eng. Chem. Res.*, 2020, **59**, 12065–12074.
54 X. Zheng, A. Than, A. Ananthanaraya, D. Kim and P. Chen, *ACS Nano*, 2013, **7**, 6278–6286.
55 Y. Zhang, J. Feng, M. He, J. Jiang, T. Xu, L. Zhou, W. Chen, W. Xiang and X. Liang, *RSC Adv.*, 2017, **7**, 49542–49547.
56 K. Qian, H. Guo, G. Chen, C. Ma and B. Xing, *Sci. Rep.*, 2018, **8**, 7991.
57 L. Liu, B. Liu, Y. Hao, J. Wang, X. Xu and X. Shang, *J. Pharm. Biomed. Anal.*, 2024, **239**, 115876.
58 A. Mishra and S. Bhattacharya, *ChemistrySelect*, 2024, **39**, 9.
59 M. Mathlouthi and D. Vinh Luu, *Carbohydr. Res.*, 1980, **81**, 203–212.
60 Y. Chen, C. Kao, P. Huang, C. Hsu and C. Kuei, *RSC Adv.*, 2016, **6**, 103006–103011.
61 S. Kim, D. Shin, C. Oh Kim, S. Kang, S. Joo, S. Choi, S. Hwang and C. Sone, *Appl. Phys. Lett.*, 2013, **102**, 053108.
62 S. Bhattacharya, R. S. Phatake, S. Nabha Barnea, N. Zerby, J.-J. Zhu, R. Shikler, N. G. Lemcoff and R. Jelinek, *ACS Nano*, 2019, **13**, 1433–1442.
63 P. Das, S. Pramanik, S. Chatterjee, A. Roy, A. Saha, S. Devi and G. Kumar, *ACS Sustainable Chem. Eng.*, 2018, **6**, 10127–10139.
64 L. Tao, Y. Yang, H. Wang, Y. Zheng, H. Hao, W. Song, J. Shi, M. Huang and D. Mitlin, *Energy Storage Mater.*, 2020, **27**, 212–225.
65 G. Ashraf, M. Asif, Ay. Aziz, A. Q. Dao, T. Zhang, T. Iftikhar, Q. Wang and H. Liu, *Nanoscale*, 2020, **12**, 9014–9023.
66 P. K. Mubari, T. Beguerie, M. Monthioux, E. Weiss-Hortala, A. Nzihou and P. Puech, *C*, 2022, **8**, 4.
67 O. Mykhailiv, H. Zubyk, K. Brzezinski, M. Gras, G. Lota, M. Gniadek, E. Romero, L. Echegoyen and M. E. Plonska-Brzezinska, *ChemNanoMat*, 2017, **3**, 583–590.
68 R. Duarah and N. Karak, *Ind. Eng. Chem. Res.*, 2019, **58**, 16307–16319.
69 J. R. Mihelcic, R. O. Barra, B. W. Brooks, M. L. Diamond, M. J. Eckelman, J. M. Gibson, S. Guidotti, A. Ikeda-Araki, M. Kumar, Y. Maiga, J. McConville, S. L. Miller, V. Pizarro, F. Rosario-Ortiz, S. Wang and J. B. Zimmerman, *Environ. Sci. Technol.*, 2023, **57**, 3457–3460.
70 T. Schuler, T. Kimura, T. Schmidt and F. Büchi, *Energy Environ. Sci.*, 2020, **13**, 2153–2166.
71 N. Dubouis and A. Grimaud, *Chem. Sci.*, 2019, **10**, 9165–9181.
72 D. Strmcnik, M. Uchimura, C. Wang, R. Subbaraman, N. Danilovic, D. van der Vliet, A. P. Paulikas, V. Stamenkovic and Ne. Markovic, *Nat. Chem.*, 2013, **5**, 300–306.
73 A. Kütt, S. Tshepelevitsh, J. Saame, M. Lõkov, I. Kaljurand, S. Selberg and I. Leito, *Eur. J. Org. Chem.*, 2021, 1407–1419.
74 W. Sheng, Z. Zhuang, M. Gao, J. Zheng, J. G. Chen and Y. Yan, *Nat. Commun.*, 2015, **6**, 5848.

